Cosmogenic production of ^{39}Ar and ^{37}Ar in argon

R. Saldanha,[1,*] H. O. Back,[1] R. H. M. Tsang,[1] T. Alexander,[1] S. R. Elliott,[2] S. Ferrara,[1] E. Mace,[1] C. Overman,[1] and M. Zalavadia[1]

[1]*Pacific Northwest National Laboratory, Richland, Washington 99352, USA*

[2]*Los Alamos National Laboratory, Los Alamos, New Mexico 87545, USA*

(Received 2 April 2019; revised manuscript received 27 May 2019; published 12 August 2019)

We have experimentally determined the production rate of ^{39}Ar and ^{37}Ar from cosmic ray neutron interactions in argon at sea level. Understanding these production rates is important for argon-based dark matter experiments that plan to utilize argon extracted from deep underground because it is imperative to know what the ingrowth of ^{39}Ar will be during the production, transport, and storage of the underground argon. These measurements also allow for the prediction of ^{39}Ar and ^{37}Ar concentrations in the atmosphere which can be used to determine the presence of other sources of these isotopes. Through controlled irradiation with a neutron beam that mimics the cosmic ray neutron spectrum, followed by direct counting of ^{39}Ar and ^{37}Ar decays with sensitive ultralow background proportional counters, we determined that the production rate from cosmic ray neutrons at sea level is expected to be (759 ± 128) atoms/(kg_{Ar}day) for ^{39}Ar, and (51.0 ± 7.4) atoms/(kg_{Ar}day) for ^{37}Ar. We also performed a survey of the alternate production mechanisms based on the state of knowledge of the associated cross sections to obtain a total sea-level cosmic ray production rate of (1048 ± 133) atoms/(kg_{Ar}day) for ^{39}Ar, (56.7 ± 7.5) atoms/(kg_{Ar}day) for ^{37}Ar in underground argon, and (92 ± 13) atoms/(kg_{Ar}day) for ^{37}Ar in atmospheric argon.

DOI: 10.1103/PhysRevC.100.024608

I. INTRODUCTION

Argon is a widely used medium for the detection of ionizing radiation. It has a high scintillation and ionization yield, allows for the propagation of scintillation photons and ionization electrons over large distances, and can be easily purified to remove non-noble impurities. Argon is therefore employed as the active medium for large neutrino detectors [1,2], scintillation vetos [3], and direct-detection dark matter experiments [4–6]. Argon is particularly attractive for dark matter detectors as the time profile of the scintillation light enables pulse-shape discrimination (PSD) of signal-like nuclear recoils from radiogenic electron recoils.

Argon is the third-most abundant gas in Earth's atmosphere, comprising roughly 0.93% of the atmosphere by volume. Argon extracted from the atmosphere consists primarily of the stable isotopes ^{40}Ar, ^{36}Ar, and ^{38}Ar. However, because of interactions of cosmic rays, atmospheric argon also contains three long-lived radioactive isotopes: ^{39}Ar, ^{37}Ar, and ^{42}Ar. The abundances and specific activity of the different isotopes in the atmosphere are given in Table I. In this paper we will focus on the two radioisotopes that, because of their high specific activity, are most relevant for argon-based dark matter experiments: ^{37}Ar and ^{39}Ar.

^{39}Ar is a pure β emitter with an endpoint of 565 keV and a half-life of 268 years [13]. For large or low background argon-based detectors ^{39}Ar is often the dominant source of interactions at low energies. The β decays of ^{39}Ar limit the sensitivity to rare events and can also create difficulties through signal pileup and high data acquisition rates. In dark matter detectors PSD is extremely effective at reducing the ^{39}Ar background at high energies, but at low energies the discrimination power is limited by the detected photon statistics and the energy threshold is often determined by the ^{39}Ar rate [6,14].

To mitigate the effects of ^{39}Ar, the next generation of argon-based dark matter detectors propose to use argon extracted from deep underground. The DarkSide-50 collaboration has demonstrated that underground argon (UAr) they are using as their dark matter target has an ^{39}Ar rate of 7.3×10^{-4} Bq/kg_{Ar} [15], a factor ≈1400 below atmospheric levels. The use of UAr rather than atmospheric argon (AAr) has allowed for a reduction in energy threshold and increase in nuclear recoil acceptance while maintaining a background-free WIMP dark matter search [5,15]. Additionally, the use of low radioactivity UAr is critical for low-mass dark matter searches which extend to lower energy thresholds than the standard WIMP search [16]. The need for argon with low levels of ^{39}Ar grows as future dark matter experiments move towards tonne-scale target masses and beyond. The relative background contributions of radioactive contaminants in external components will decrease because of self-shielding of the argon and a decreasing surface-to-volume ratio, making ^{39}Ar (which scales with the target mass) the likely dominant background.

Similar to the commercial production of argon from the atmosphere, UAr must be extracted from crude naturally

*richard.saldanha@pnnl.gov

TABLE I. Stable and long-lived isotopes of argon, along with their typical abundances [12] and specific activity in atmospheric argon.

Isotope	Abundance	Specific activity (Bq/kg_{Ar})
^{40}Ar	0.9960	Stable
^{36}Ar	0.0033	Stable
^{38}Ar	0.0006	Stable
^{39}Ar	8.2×10^{-16}	1.0 [7,8]
^{37}Ar	$\approx 1.3 \times 10^{-20}$	$\approx 4.5 \times 10^{-2}$ [9]
^{42}Ar	6.8×10^{-21}	6.8×10^{-5} [10,11]

occurring gases underground. In the case of the DarkSide-50 experiment this crude gas is primarily CO_2, extracted from a gas well in Cortez, Colorado [17]. The processing, transport, and storage of the UAr on the surface of Earth exposes the UAr to cosmic rays until it can be suitably shielded underground. Given the extremely stringent requirements on the levels of ^{39}Ar for dark matter detectors, cosmogenic production of ^{39}Ar in the UAr is an important concern.

^{37}Ar decays purely through electron capture, producing low energy x rays and Auger electrons, with a relatively short half-life of 35.01 days [18]. Because low background experiments are typically operated deep underground, shielded from cosmic rays, the ^{37}Ar activity typically decays below measurable levels within a few months, though the x-ray peak can be used as a low energy calibration source during early data taking [16]. ^{37}Ar can also be produced by underground nuclear explosions through neutron reactions with calcium in the soil [19]. Elevated rates of ^{37}Ar in the environment are a strong indicator of a nuclear explosion and can therefore be used to verify compliance with nuclear test ban treaties. Thus the natural cosmogenic production of ^{37}Ar in the atmosphere and surface soil gas acts as a background to underground nuclear monitoring [20].

The cosmogenic production of both ^{37}Ar and ^{39}Ar in argon is expected to be dominated by neutron-induced reactions but there are no existing measurements of the total production cross section or integrated cosmogenic production rate. Estimates for dark matter experiments have therefore had to rely on semiempirical calculations, which as we show, significantly underestimate the production rates. In this paper we describe a measurement of the integrated production rate from a neutron beam at the Los Alamos Neutron Science Center (LANSCE) Ice House facility [22,23] which has a very similar energy spectrum to that of cosmic ray neutrons at sea level (see Fig. 1). While the spectral shape is similar, the neutron beam has a flux that is $\approx 4.5 \times 10^8$ times higher above 10 MeV, which allows for the production of measurable amounts of ^{39}Ar in short periods of time. We irradiated samples of underground and atmospheric argon for 3 days on the neutron beam and then measured the resulting activity in ultralow background gas proportional counters (ULBPC) at Pacific Northwest National Laboratory (PNNL). The ULBPCs are custom built to detect low levels of ^{39}Ar and ^{37}Ar in gas samples for the purpose of radiometric dating and support of future nuclear test ban treaty monitoring [24], with a

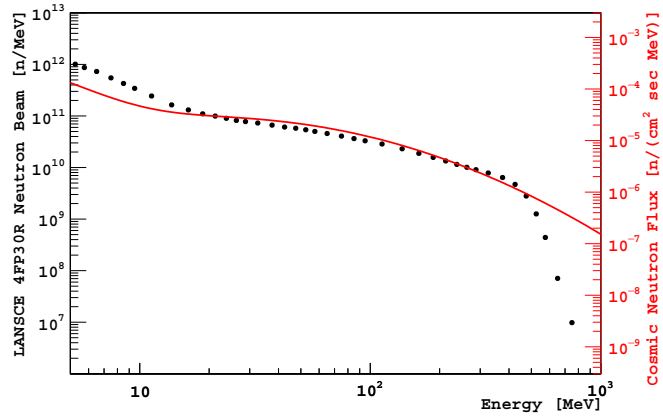

FIG. 1. Comparison of the LANSCE 4FP30R neutron beam with sea-level cosmic ray neutrons. The black data points and left vertical axis show the number of neutrons measured by the fission chamber during the 3-day beam exposure used for this measurement. The red continuous line and the right vertical axis show the reference cosmic ray neutron flux at sea level for New York City during the midpoint of solar modulation [21].

sensitivity to ^{39}Ar at the level of 2.5×10^{-2} Bq/kg_{Ar} [25,26] and to ^{37}Ar at the level of 4.3×10^{-3} Bq/kg_{Ar} [19,26]. The high intensity of the LANSCE neutron beam and the sensitivity of the ULBPC detectors allow us to experimentally measure the ^{39}Ar and ^{37}Ar production rate and extrapolate them to estimate the sea-level cosmogenic neutron production rate.

II. ^{39}Ar PRODUCTION MECHANISMS

The production of ^{39}Ar in the atmosphere is primarily from cosmic rays. While several of the production channels do not have measured cross sections, based on the known flux of the various cosmogenic particles and the general behavior of cross sections for similar isotopes, it is estimated that interactions with fast neutrons account for more than 94% of the total ^{39}Ar production in the atmosphere [7]. There are two[1] primary fast neutron reactions that result in the production of ^{39}Ar : ^{40}Ar (n, 2n)^{39}Ar and ^{40}Ar[(n, np) + (n, pn) + (n, d)] ^{39}Cl. In the latter case, which we will henceforth abbreviate to ^{40}Ar (n, d)^{39}Cl, the short-lived ^{39}Cl decays to ^{39}Ar through β decay with a 55.6-min half-life. Because ^{39}Ar is a pure β emitter it is not possible to directly measure the total production cross section by conventional methods that rely on γ-ray detectors to tag the reaction products. The only existing measurements are of the partial cross sections ^{40}Ar(n, 2nγ)^{39}Ar to excited states of ^{39}Ar [27] and of ^{40}Ar (n, d)^{39}Cl through the detection of gamma rays from the ^{39}Cl decay [28–31].

Estimates of the cosmogenic activation rates have therefore had to rely on either semiempirical calculations such as the Silberberg and Tsao equations [32–37] that are employed

[1]The neutron-induced production of ^{39}S, which sequentially decays to ^{39}Cl and ^{39}Ar, is estimated to be 4 orders of magnitude smaller than the direct ^{39}Ar production. For other possible production mechanisms see Sec. VII.

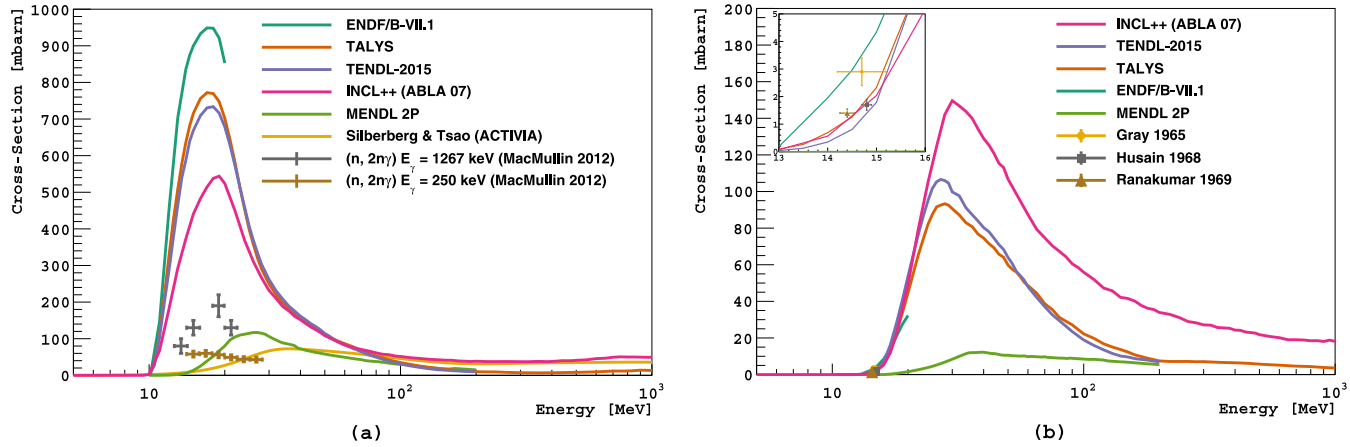

FIG. 2. Estimates (continuous lines) and experimental measurements (data points) of ^{39}Ar production cross sections from ^{40}Ar. (a) ^{40}Ar (n, 2n)^{39}Ar cross sections. Note that the experimental measurements are partial cross sections to excited states of ^{39}Ar [27]. (b) ^{40}Ar (n, d)^{39}Cl cross sections with experimental measurements at ≈14.6 MeV [28–30]. The Silberberg and Tsao (n, d) cross section calculated by ACTIVIA is combined with the (n, 2n) cross section shown in (a).

by codes such as YIELDX [38], COSMO [39], and ACTIVIA [40], Monte Carlo simulations of the hadronic interactions between nucleons and nuclei that are performed by codes such as INCL [41], ABLA [42], TALYS [43], etc., or compiled databases that combine calculations with experimental data such as ENDF [44], MENDL-2P [45], and TENDL [46]. The ^{39}Ar production cross section estimates from some of these different methods,[2] along with the experimentally measured partial cross sections, are shown in Fig. 2. It can be seen that the estimates vary by up to an order of magnitude at certain energies, yielding similar sized variation in the predicted ^{39}Ar production rate. It should be noted that previous estimates of the cosmogenic activation rate of underground argon [50] have used the Silberberg and Tsao semiempirical calculations as implemented in the COSMO and ACTIVIA codes, which have the lowest predicted cross sections and are significantly below the experimentally measured partial cross sections.

III. ^{37}Ar PRODUCTION MECHANISMS

The production of ^{37}Ar in the atmosphere is also dominated by neutron interactions on argon. Previous calculations [51] estimate that 93% of the total production in the troposphere is from fast neutrons through ^{40}Ar (n, 4n)^{37}Ar, with the remaining fraction[3] from the capture of thermal and epithermal neutrons through ^{36}Ar(n, γ)^{37}Ar. The only detectable signal from ^{37}Ar decays are the low-energy x rays and Auger electrons following the electron capture, and thus the ^{40}Ar (n, 4n)^{37}Ar production cross section cannot be measured with γ-ray detectors. To our knowledge there are no known experimental measurements of this cross section. Examples of estimates from semiempirical calculations, simulations, and evaluated databases are shown in Fig. 3. As with the ^{39}Ar production cross sections, these estimates can vary by up to an order of magnitude.

IV. EXPERIMENT

Three samples of argon gas were prepared for irradiation, two UAr samples and one AAr sample. The UAr samples were taken from the same source of gas that was used in the DarkSide-50 experiment and the AAr sample was commercial ultrahigh purity (99.999%) grade argon obtained from Oxarc. An AAr sample was used in addition to the UAr samples to investigate if the different isotopic composition of the gases would lead to significantly different ^{39}Ar and ^{37}Ar production. In addition to ^{40}Ar, AAr contains ^{36}Ar at 0.334% and ^{38}Ar at 0.063% [12,52]. UAr is composed almost solely of ^{40}Ar with the ^{36}Ar concentration measured by mass spectrometry to

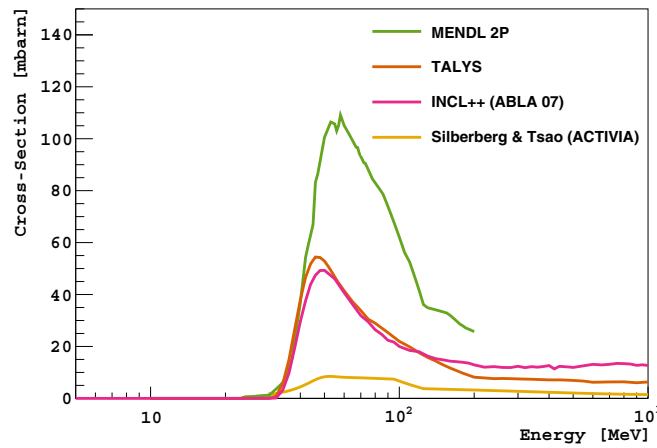

FIG. 3. Estimates of ^{37}Ar production cross sections from ^{40}Ar. There are no known experimental measurements.

[2]The Silberberg and Tsao, and MENDL-2P cross sections were obtained from the ACTIVIA code package [47], the INCLXX cross sections were calculated using the INCL++ code (v6.0.1) with the ABLA07 de-excitation model [48], and the TALYS cross sections calculated using TALYS-1.9 [49]. The default parameters were used for all programs.

[3]For other possible production mechanisms see Sec. VII.

TABLE II. Central values and uncertainties of the parameters and experimentally measured values used to determine the beam-induced ^{39}Ar and ^{37}Ar activity in UAr cylinder II and AAr cylinder III. See text for details.

	UAr cylinder II		AAr cylinder III	
	Value	Unc.(%)	Value	Unc.(%)
Atomic weight [12]	$39.9624^{+0}_{-0.003}$	7×10^{-3}	$39.947\,80 \pm 0.000\,02$	3.8×10^{-5}
^{40}Ar isotopic abundance [12]	$1.0000^{+0}_{-0.0007}$	0.07	$0.996\,035 \pm 0.000\,004$	4.2×10^{-4}
Mass (g)	3.603 ± 0.084	2.3	3.626 ± 0.084	2.3
^{40}Ar areal density (atoms/cm^2)	$(1.218 \pm 0.020) \times 10^{21}$	1.6	$(1.219 \pm 0.020) \times 10^{21}$	1.6
Neutrons (>10 MeV) through cylinder	$(9.03 \pm 0.54) \times 10^{12}$	5.9	$(8.77 \pm 0.53) \times 10^{12}$	6.0
ULBPC sample mass (g)	1.070 ± 0.011	1.0	1.052 ± 0.011	1.0
ULBPC ^{39}Ar activity (mBq)	46.12 ± 0.46	1.0	43.96 ± 0.46	1.0
ULBPC ^{37}Ar activity (mBq)	216.3 ± 6.8	3.1	90.07 ± 2.80	3.1
^{39}Ar half-life (years) [13]	268 ± 8	3	268 ± 8	3
Pre-existing ^{39}Ar activity (mBq)	$(4.3 \pm 0.4) \times 10^{-3}$	9.5	3.7 ± 0.3	8.5
Beam-averaged cross section (cm^2)	$(1.72 \pm 0.12) \times 10^{-25}$	7.2	$(1.67 \pm 0.12) \times 10^{-25}$	7.3
Beam-induced ^{39}Ar activity (mBq)	$\mathbf{155.4 \pm 4.2}$	**2.7**	$\mathbf{146.7 \pm 4.1}$	**2.8**
^{37}Ar half-life (d) [18]	35.011 ± 0.019	0.054	35.011 ± 0.019	0.054
^{37}Ar decay correction factor	$(2.7996 \pm 0.0061) \times 10^{-2}$	0.22	$(1.2205 \pm 0.0032) \times 10^{-2}$	0.26
Pre-existing ^{37}Ar activity (Bq)	$(1.6 \pm 0.5) \times 10^{-4}$	33	$(1.6 \pm 0.5) \times 10^{-4}$	33
Beam-averaged cross section (cm^2)	$(1.033 \pm 0.074) \times 10^{-26}$	7.2	$(1.031 \pm 0.075) \times 10^{-26}$	7.3
Beam-induced ^{37}Ar activity (Bq)	$\mathbf{26.0 \pm 1.0}$	**4.0**	$\mathbf{25.3 \pm 1.0}$	**4.0**

be less than 0.01% and the ^{38}Ar concentration expected to be reduced by a similar factor compared to AAr, consistent with measurements of gas extracted from deep underground wells [7]. For the sake of clarity, all numbers and uncertainties related to the gas samples in the main body of this paper refer to one of the UAr samples (cylinder II). The corresponding numbers for the AAr sample (cylinder III) are included in Table II, while the other UAr sample (cylinder I) was kept as contingency and not measured.

The gas samples were filled at 1.12 bar and 296 K in three identical aluminum cylinders, each with an interior volume of 1.96 L (calculated through calibrated volume-ratio measurements), corresponding to (3.60 ± 0.08) g of gas, where the uncertainty includes the uncertainties in pressure, temperature, and volume. The custom-designed cylinders had a nominal 76.2-mm (3-inch) internal diameter and 439-mm internal length and were fabricated from aluminum to minimize the attenuation of the neutron beam as well as activation of the cylinder material. The end caps of the cylinder, through which the neutron beam passed, had a thinned (1.5 ± 0.1)-mm-thick central wall and were welded onto the cylindrical section. The gas was filled and emptied through a single 6.35-mm diameter double-valved tube on each cylinder and the cylinders were evacuated to $\approx 1 \times 10^{-6}$ bar before being filled with the argon gas sample.

The samples were irradiated at the LANSCE WNR ICE-HOUSE II facility [23] on Target 4 Flight Path 30 Right (4FP30R). A broad-spectrum (0.2–800 MeV) neutron beam was produced via spallation of 800-MeV protons on a tungsten target. A 50.8-mm (2-inch) diameter beam collimator was used to restrict the majority of the neutrons to within the diameter of the gas cylinder. The neutron fluence was measured with ^{238}U foils by an in-beam fission chamber [54] placed downstream of the collimator. The beam has a pulsed time structure which allows the incident neutron energies to be determined using a time-of-flight (TOF) measurement between the proton beam pulse and the fission chamber signals [22,54]. As shown in Fig. 4, the three gas cylinders were placed end to end with the two UAr cylinders (I and II) closest to the fission chamber and AAr cylinder III furthest away. The closest end of the UAr cylinder I was located 791 mm downstream from the fission chamber.

The beam exposure took place over three days between December 11 and 14, 2017. The fluence measured by the fission chamber is shown in Fig. 1, with a total of $(1.03 \pm 0.05) \times 10^{13}$ neutrons above 10 MeV. The uncertainty is

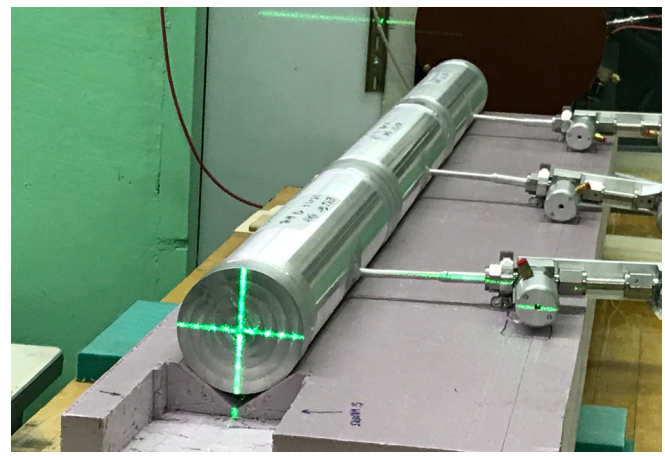

FIG. 4. Picture of the three argon gas cylinders placed on the Target 4 Flight Path 30 Right (4FP30R) at the LANSCE WNR ICE-HOUSE II facility. The beam direction is out of the page and the laser used for alignment of the cylinders can be seen on the face of the AAr cylinder III, which is furthest downstream.

dominated by the systematic uncertainty in the ^{238}U(n, f) cross section which varies from 2% to 5% below 200 MeV [55] (which includes most of the production range) and we have conservatively assumed 5% across the whole spectrum. The uncertainty in the neutron energy spectrum because of the timing uncertainty in the TOF measurement (1.2 ns) is negligible for this measurement. While the nominal beam diameter was set by the 2-inch collimator, the cross-sectional beam profile has significant tails at larger radii, with roughly 10% falling outside the 3-inch diameter of the gas cylinders. Additionally the beam is slightly diverging, with an estimated cone opening angle of 0.233°. A GEANT4 [56,57] simulation that included the measured beam profile and beam divergence, the measured neutron spectrum, and the full geometry and materials of the gas cylinder, was used to calculate the neutron fluence through each cylinder. The estimated reduction factor of the neutron fluence through UAr cylinder II in the 10–200 MeV range, compared to the fluence measured by the fission chamber, is 0.876 ± 0.028, where the uncertainty includes the uncertainty in the beam profile and a $\pm 0.25''$ uncertainty in the alignment of the beam center with the cylinder axes.

Following the irradiation the cylinders were stored for a cool-down period of roughly a month before they were shipped to PNNL for counting. The measured pressure of the argon in the irradiated cylinders upon return to PNNL matched the initial fill pressures within uncertainties, indicating that no argon had leaked out during the transportation or irradiation. Activation calculations indicated that along with ^{39}Ar and ^{37}Ar, several other long-lived radioisotopes would also be produced by the irradiation, most notably ^{32}P, ^{33}P, ^{35}S, ^{22}Na, ^{3}H, and ^{7}Be. However, previous experiments involving the irradiation of argon [58,59] found that activation products remain in the irradiation canister when argon is transferred out. Because tritium is especially dangerous as it can introduce a long-lived radioactive background into the ULBPC , the argon gas was cryopumped through a hydrogen getter into a smaller cylinder for loading into the ULBPC . The irradiated gas was then mixed with 10% methane to form P-10 count gas.

A sample of the P-10 gas mixture from the UAr cylinder II was loaded into the 100.5 cm^3 ULBPC at 6.44 bar and 295 K, corresponding to an argon mass of 1.07 g. The irradiated UAr gas was counted for 31.8 days at low gain to measure the ^{39}Ar spectrum from 15 to 400 keV and was also counted at high gain from 0 to 15 keV for 3.91 d to measure the 3-keV ^{37}Ar peak.

The ^{39}Ar detection efficiency of the ULBPC detector was calibrated with a 62.6 mBq ^{39}Ar source [53], and a 15.6-d background run was also acquired. As shown in Fig. 5, the extremely good agreement in spectral shape between the efficiency spectrum and the data indicate that no other β-decaying activation products were present in the gas sample. After subtracting the measured background spectrum and accounting for the calibrated detection efficiency of 0.688 ± 0.003, the measured ^{39}Ar activity in the ULBPC was found to be (46.1 ± 0.5) mBq.

For ^{37}Ar, the spectrum was fit with a Gaussian to represent the ≈2.8-keV Auger electrons and x rays following a K-shell

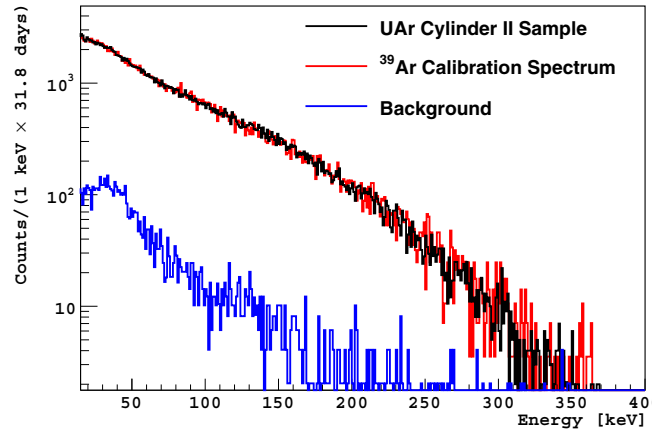

FIG. 5. Energy spectrum from gas in irradiated UAr cylinder II (black) as measured by the ULBPC at low gain. The spectrum from a ^{39}Ar calibration sample [53] is overlaid for comparison (red) along with a background spectrum (blue).

electron capture and an exponential decay for the underlying ^{39}Ar spectrum (shown in Fig. 6). The branching ratio for the K-shell electron capture is $(90.2 \pm 0.2)\%$ [18,60] and the combined ULBPC fiducial volume efficiency for both Auger electrons and x rays is 0.79 ± 0.02 [61]. Including systematic uncertainties from the choice of fit range and response function we obtained a total measured ^{37}Ar activity in the ULBPC of (216 ± 7) mBq, scaled to the start of the counting time (accounting for the decay of ^{37}Ar during the measurement period).

Scaling these activities by the fraction of the total irradiated gas measured and the radioactive decay between the start of the irradiation and the measurement, we found an ^{39}Ar activity of (155 ± 4) mBq and an ^{37}Ar activity of (26.0 ± 1.0) Bq for all the gas in the irradiated UAr cylinder II. Following the same procedure described above, for the gas from AAr

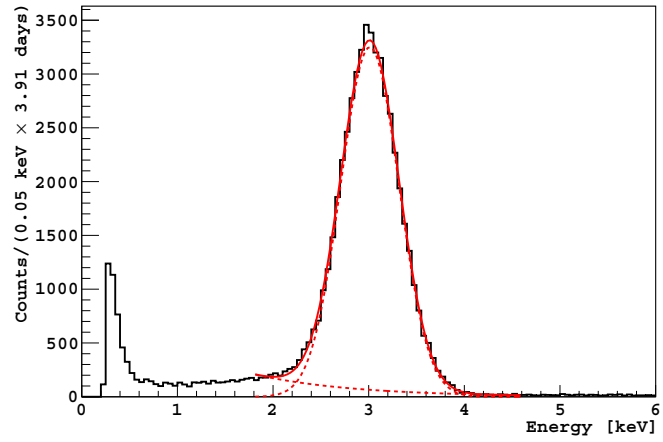

FIG. 6. Energy spectrum from gas in irradiated UAr cylinder II (black) as measured by the ULBPC at high gain. The peak region around 3 keV is fit (red solid) with a Gaussian (representing the ^{37}Ar Auger electrons and x rays) and a falling exponential (for the underlying background).

cylinder III we found an ^{39}Ar activity of (150 ± 4) mBq and an ^{37}Ar activity of (25.3 ± 1.0) Bq.

One must also account for the cosmogenic ^{39}Ar and ^{37}Ar activity that is present in the samples even without the beam irradiation. Atmospheric argon was found to contain a specific activity of (1.01 ± 0.08) Bq/kg$_{\mathrm{Ar}}$ [8] of ^{39}Ar, corresponding to an activity of (3.7 ± 0.3) mBq in AAr cylinder III, which must be subtracted from the measured activity when calculating the beam activation rate. The UAr sample was obtained from the same source of gas used by DarkSide-50 that was found to have an ^{39}Ar specific activity of (0.73 ± 0.11) mBq/kg$_{\mathrm{Ar}}$. Compared to the DarkSide-50 target which was transported deep underground in February 2015, our UAr samples spent approximately 1170 additional days on the surface, exposed to cosmic rays. Even assuming the highest considered cross section, the total pre-existing rate of ^{39}Ar in the irradiated gas sample is roughly 4.3 μBq, negligible compared to the measured activity.

For the short-lived ^{37}Ar, both samples will have reached equilibrium activity from cosmogenic production at sea level. Measurements of the ^{37}Ar activity in the low troposphere (excluding variations from in-flows of stratospheric air, outgassing of soil air, and emissions from nuclear installations) indicate an equilibrium value of 0.5–1.0 mBq/m^3 air (30–60 mBq/kg$_{\mathrm{Ar}}$) [9]. The equilibrium rate at sea level is expected to be significantly lower than the rate averaged over the troposphere [in Sec. VII we estimate it to be (0.7–1.1 mBq/kg$_{\mathrm{Ar}}$)], but we conservatively use the averaged tropospheric value as an upper limit, corresponding to total activity of $(1.6 \pm 0.5) \times 10^{-4}$ Bq, which is in any case negligible compared to the measured activity.

The final estimates for the beam-induced activity in the UAr [AAr] sample at the end of the irradiation are (155 ± 4) mBq [(147 ± 4) mBq] ^{39}Ar and (26 ± 1) Bq [(25 ± 1) Bq] ^{37}Ar. The specific input values used as well as the included statistical and systematic uncertainties are listed in Table II. To compare the results between the UAr and AAr samples we can divide the measured activity by the total number of neutrons and target ^{40}Ar atoms to obtain a beam-averaged cross section (listed in Table II). The ratio of the UAr to AAr beam-averaged cross section, after eliminating common systematic uncertainties, is 1.029 ± 0.055 and 1.002 ± 0.052 for ^{39}Ar and ^{37}Ar, respectively. The good agreement between the irradiated UAr and AAr activities indicate that, as expected, there was no appreciable contribution from neutron interactions with the small fractions of naturally occurring ^{36}Ar and ^{38}Ar isotopes present in the AAr sample. The agreement also verifies the accuracy of the simulations of the beam attenuation between the targets and the independent ULBPC activity measurements.

V. CROSS SECTIONS

If the neutron beam had an energy spectrum identical to that of the cosmic ray neutron flux we could simply estimate the cosmogenic production rate by scaling the measured activity by the ratio of the cosmic-ray neutrons to that of the neutron beam. However, the beam spectrum falls off faster at higher energies than that of cosmic rays (see Fig. 1). Thus we must rely on a model for the production cross sections to extrapolate from the beam measurement to the cosmogenic production rate.

We can evaluate the accuracy of the different cross-section models by comparing the predicted ^{39}Ar and ^{37}Ar production rates from the LANSCE neutron beam irradiation to the measured rates. The number of isotopes atoms $N(t)$ at a given time t is governed by the equation,

$$\frac{dN}{dt} = +P(t) - \frac{N(t)}{\tau}, \tag{1}$$

where τ is the mean life (s) of the isotope decay and $P(t)$ is the isotope production rate (atoms/s). Ignoring any existing isotope concentration (subtracted off from the measured experimental value), the measured decay rate at any time after the start of the beam irradiation is given by

$$D(t) \equiv \frac{N(t)}{\tau} = \frac{e^{-\frac{t}{\tau}}}{\tau} \int_0^t P(t') e^{\frac{t'}{\tau}} dt'. \tag{2}$$

For a given cross-section model $\sigma(E)$ (cm^2),

$$P(t) = n_a \int S(E,t)\sigma(E)\, dE, \tag{3}$$

where n_a is the areal number density of the target argon atoms (atoms/cm^2) and $S(E,t)$ is the energy spectrum of neutrons (neutrons/(MeV s)). The second column of Table III shows the calculated values for the different ^{39}Ar cross-section models considered, with the corresponding numbers for ^{37}Ar shown in Table IV. We note that not all the cross-section models considered span the entire range of neutron energies. The TENDL 2015 and MENDL-2P cross sections are only reported up to 200 MeV, while the TALYS cross sections have been extended up to 1 GeV [62]. The INCL++ model can handle neutron-induced reactions up to 15–20 GeV, while the Silberberg and Tsao semiempirical cross-section calculations implemented in ACTIVIA can be performed at any energy, although the cross sections are assumed to be independent of energy above $\approx$3 GeV.

From the ratio of the experimentally measured values to the predictions (shown in the third column of Tables III and IV) it can be seen that the TENDL-2015, TALYS, and INCL++ models all predict ^{39}Ar activities within 10% of the measured LANSCE activation value. However, the Silberberg and Tsao cross-section model used as the default by the ACTIVIA and COSMO codes, and previously used to estimate the cosmogenic production rate for argon dark matter experiments [50], predict values more than a factor of 4 smaller than the experimental measurement. The predictions for the ^{37}Ar production vary from the experimental measurements by roughly a factor three in both directions, with the TALYS and INCL++ models accurate to within about 50%.

If we assume that the shape of the cross-section model as a function of energy is correct, the ratio of the experimentally measured activity to the predicted activity represents the normalization factor that will need to be applied to each model to best match the experimental data. In the next section we will use this ratio to estimate the ^{37}Ar and ^{39}Ar production rates from cosmic ray neutrons.

TABLE III. ^{40}Ar (n, 2n)^{39}Ar and ^{40}Ar (n, d)^{39}Cl production rates for different cross-section models. The second and fourth column show the predicted rates for the LANSCE neutron beam exposure and sea-level cosmic ray neutrons, respectively. The third column shows the ratio of the neutron beam prediction to the experimental measurement while the final column shows the cosmogenic production rate scaled by that ratio.

Cross-section model	Pred. LANSCE ^{39}Ar activity (mBq)	Meas./Pred. LANSCE ^{39}Ar activity	Pred. cosmogenic ^{39}Ar prod. rate [atoms/(kg$_{Ar}$day)]	Scaled cosmogenic ^{39}Ar prod. rate [atoms/(kg$_{Ar}$day)]
Silberberg & Tsao (ACTIVIA)	37.1 ± 2.5	4.19 ± 0.31	200 ± 25	840 ± 120
MENDL-2P	36.0 ± 2.5	4.31 ± 0.32	188 ± 24	810 ± 120
TENDL-2015	162 ± 11	0.961 ± 0.071	726 ± 91	700 ± 100
TALYS	168 ± 12	0.924 ± 0.068	753 ± 94	700 ± 100
INCL++ (ABLA07)	172 ± 12	0.902 ± 0.067	832 ± 104	750 ± 110

VI. PRODUCTION RATES FROM FAST COSMIC RAY NEUTRONS

There have been several measurements and calculations of the cosmic ray neutron flux (for, e.g., [63–65]). The intensity of the neutron flux varies with altitude, location in the geomagnetic field, and solar magnetic activity (though the spectral shape does not vary as significantly) and correction factors must be applied to calculate the appropriate flux [66]. The most commonly used reference spectrum for sea-level cosmic ray neutrons is the so-called "Gordon" spectrum [21] (shown in Fig. 1), which is based on measurements at five different sites in the United States, scaled to sea level at the location of New York City during the midpoint of solar modulation. We have used the parametrization given in [21] which agrees with the data to within a few percent. The spectrum uncertainties at high energies are dominated by uncertainties in the spectrometer detector response function (<4% below 10 MeV and 10%–15% above 150 MeV) and we have assigned an average uncertainty of 12.5%.

The production rate per unit target mass P' [atoms/(kg$_{Ar}$ s)] of isotopes from the interaction of cosmic ray neutrons can be written as

$$P' = n \int \Phi(E)\sigma(E)\, dE, \tag{4}$$

where n is the number of target atoms per kilogram of argon and $\Phi(E)$ is the cosmic neutron flux [neutrons/(cm^2 s MeV)]. The integral is evaluated from 1 MeV to 10 GeV.

The predicted production rate per unit target mass for the cross-section models considered is shown in the fourth column of Tables III and IV for ^{39}Ar and ^{37}Ar, respectively. Scaling these values by the ratio of the experimental to predicted activities for the LANSCE neutron beam, we obtain our best estimates for the cosmic neutron induced production rates per unit target mass, shown in the final columns. The spread in the values for the different cross sections is an indication of the systematic uncertainty in the extrapolation from the LANSCE beam measurement to the cosmic neutron spectrum. If either the LANSCE neutron beam spectral shape was the same as that of the cosmic ray neutrons, or the cross-section models all agreed in shape, the central values in the final column would be identical. The estimated activation rate from cosmic ray neutrons is $(759 \pm 56_{exp} \pm 65_{cs} \pm 95_{nf})$ atoms(^{37}Ar)/(kg$_{Ar}$day) and $(51.0 \pm 3.8_{exp} \pm 0.6_{cs} \pm 6.4_{nf})$ atoms(^{37}Ar)/(kg$_{Ar}$day), where the first uncertainty listed is from experimental measurement uncertainties (represented by the average uncertainty on the ratio of the measured to predicted activity from the LANSCE beam irradiation for a specific cross-section model), the second is from the uncertainty in the shape of the cross-section models (calculated as the standard deviation of the scaled cosmogenic production rates by the different models), and the third is from the uncertainty in the sea-level cosmic neutron flux.

VII. ALTERNATE PRODUCTION MECHANISMS

In addition to activity induced by fast neutrons, interactions of gamma rays, muons, protons, and thermal neutrons also contribute to the total production rate of ^{39}Ar and ^{37}Ar. Previous calculations estimated that interactions of fast

TABLE IV. ^{40}Ar (n, 4n)^{37}Ar production rates for different cross-section models (TENDL-2015 cross sections were not available). The second and fourth column show the predicted rates for the LANSCE neutron beam exposure and sea-level cosmic ray neutrons, respectively. The third column shows the ratio of the neutron beam prediction to the experimental measurement while the final column shows the cosmogenic production rate scaled by that ratio.

Cross-section model	Pred. LANSCE ^{37}Ar activity (Bq)	Meas./Pred. LANSCE ^{37}Ar activity	Pred. cosmogenic ^{37}Ar prod. rate [atoms/(kg$_{Ar}$day)]	Scaled cosmogenic ^{37}Ar prod. rate [atoms/(kg$_{Ar}$day)]
Silberberg & Tsao (ACTIVIA)	9.19 ± 0.57	2.83 ± 0.21	17.9 ± 2.2	50.7 ± 7.4
MENDL-2P	79.7 ± 4.9	0.326 ± 0.024	155 ± 19	50.5 ± 7.3
TALYS	39.1 ± 2.4	0.666 ± 0.049	76.8 ± 9.6	51.1 ± 7.4
INCL++ (ABLA07)	39.9 ± 2.5	0.653 ± 0.048	79.3 ± 9.9	51.8 ± 7.5

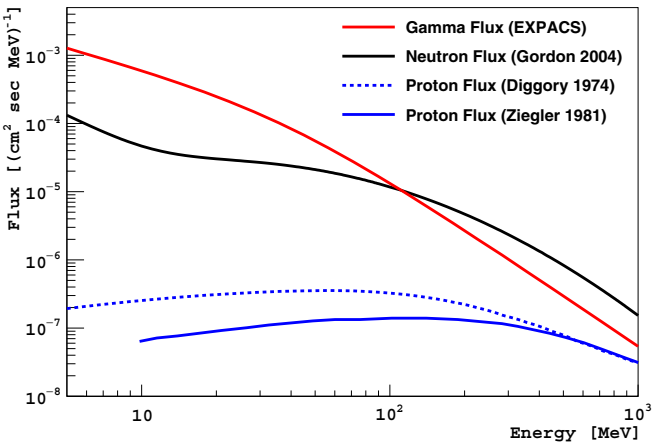

FIG. 7. Sea-level cosmic ray flux of gamma rays [67], neutrons [21], and protons [68,69].

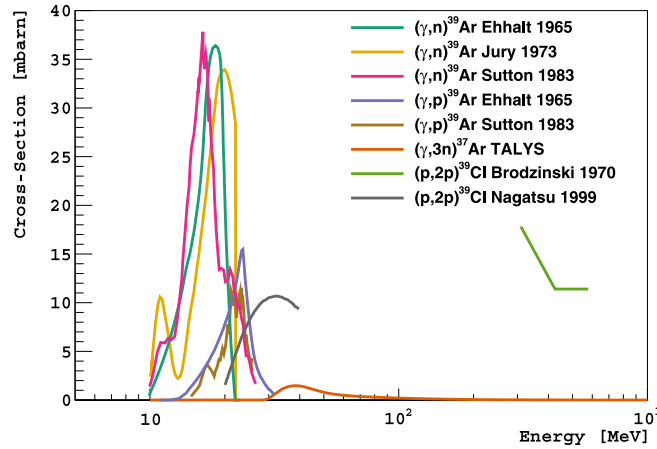

FIG. 8. Production cross sections for ^{39}Ar and ^{37}Ar on ^{40}Ar through gamma and proton interactions. See text for details and references.

neutrons account for 94% of the total ^{39}Ar production in the atmosphere [7] and 93% of the production of ^{37}Ar in the troposphere [51]. However, at Earth's surface the ratio of the fast neutron flux compared to other cosmogenic particles is significantly different because of different attenuation lengths in the atmosphere and the relative contributions must be re-evaluated. In the following two subsections we describe the methods we used to estimate the individual contributions using existing measurements and models.

A. Alternate ^{39}Ar production mechanisms

1. ^{40}Ar (μ, n)^{39}Cl

The production rate from muon captures at sea level $P_{\mu 0}$ can be estimated by

$$P_{\mu 0} = R_0 \frac{\lambda_c(^{40}\mathrm{Ar})}{\lambda_d + \lambda_c(^{40}\mathrm{Ar})} f^*(^{39}\mathrm{Cl}), \quad (5)$$

where $R_0 = 484 \pm 71\ \mu^-/(\mathrm{kg_{Ar}day})$ is the rate of stopped muons at sea level [73] and we have added a 10% uncertainty to account for the 10% difference in the (Z/A) value for argon compared to air, $\lambda_c(^{40}\mathrm{Ar}) = (1.20 \pm 0.08) \times 10^6/\mathrm{s}$ is the capture rate of muons on argon [74], $\lambda_d = 4.552 \times 10^{-5}\ \mathrm{s}^{-1}$ is the decay rate of muons [75], and $f^*(^{39}\mathrm{Cl}) = 0.490 \pm 0.014$ is the effective probability of producing ^{39}Cl or ^{39}S [76,77]. The sea-level production rate from muon captures is therefore estimated to be $(172 \pm 26)\,\mathrm{atoms/(kg_{Ar}day)}$.

2. ^{40}Ar (γ, n)^{39}Ar *and* ^{40}Ar (γ, p)^{39}Cl

The flux of high energy γ rays at Earth's surface was obtained using the PARMA analytical model [78] as implemented in the EXPACS software program [67]. Similar to the neutron spectrum, we used New York City as our reference location for the γ spectrum, which is shown in Fig. 7. We verified that the γ flux predicted by the model agreed with experimental measurements [79] to within 20% in the energy range of interest (10–30 MeV), which we used as our estimate of the systematic uncertainty. Experimental measurements of the ^{40}Ar (γ, n)^{39}Ar cross section [80–82] and the ^{40}Ar (γ, p)^{39}Cl cross section [80,82] are shown in Fig. 8. Where multiple measurements exist we have used the mean and sample standard deviation of the calculated production rates as our estimates of the central value and uncertainty. The estimates for the individual processes are shown in Table V with the total sea-level production rate from γ rays estimated to be $(113 \pm 24)\,\mathrm{atoms/(kg_{Ar}day)}$.

3. ^{40}Ar (p, 2p) ^{39}Cl *and* ^{40}Ar (p, pn)^{39}Ar

At sea level the flux of 10–100 MeV cosmic ray protons is at least 30 times lower than that of cosmic ray neutrons because of the additional electromagnetic interactions of protons in the atmosphere. To estimate the production rate from protons we have used the proton spectra from [69] and [68] (scaled by the angular distribution from the EXPACS code) as shown in Fig. 7. Measurements of the ^{40}Ar (p, 2p)^{39}Cl cross section at low [83] and high [58] energies are shown in Fig. 8 but, because of the low proton flux, the contribution to the

TABLE V. Total cosmogenic production rates of ^{39}Ar at sea level. The first row is the estimate from fast neutrons based on the measurement presented in this work, while the other rows are best estimates made from existing experimental data and models.

Reaction	Estimated ^{39}Ar production rate [atoms/(kg$_{\mathrm{Ar}}$day)]	Fraction of total AAr (%)
^{40}Ar (n, 2n)^{39}Ar+ ^{40}Ar(n, d)^{39}Cl	759 ± 128	72.3
^{40}Ar (μ, n)^{39}Cl	172 ± 26	16.4
^{40}Ar (γ, n)^{39}Ar	89 ± 19	8.5
^{40}Ar (γ, p)^{39}Cl	23.8 ± 8.7	2.3
^{40}Ar (p, 2p)^{39}Cl	<0.1	<0.01
^{40}Ar (p, pn)^{39}Ar	3.6 ± 2.2	0.3
^{38}Ar(n, γ)^{39}Ar	$\ll 0.1$ (UAr) 1.1 ± 0.3 (AAr)	– 0.1
Total	1048 ± 133	100

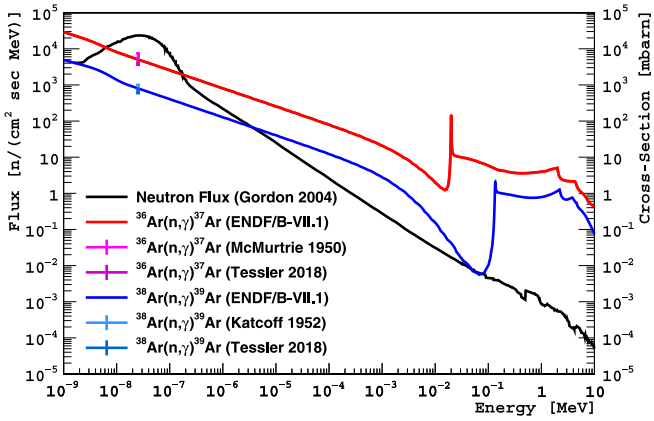

FIG. 9. Thermal and epi-thermal neutron flux (black, left axis) and capture cross sections on ^{36}Ar (red) and ^{38}Ar (blue) along with experimental data points at thermal energies [70–72].

overall production rate at sea level is negligible. We are not aware of any measurements of the ^{40}Ar (p, np)^{39}Ar cross section (again probably because of the difficulty of detecting ^{39}Ar) and have therefore based our estimates on the ^{40}Ar (n, d)^{39}Ar cross section from TALYS, scaled by the same factor used in Table III. As before, we have used the mean and sample standard deviation of the calculated production rates with the different proton spectra and cross sections as our estimates of the central value and uncertainty, yielding a sea-level production rate of (3.6 ± 2.2) atoms/(kg$_{\rm Ar}$day).

4. ^{38}Ar(n, γ)^{39}Ar

In atmospheric argon (AAr), ^{39}Ar can also be produced through the capture of thermal and epi-thermal neutrons on ^{38}Ar. For the low energy neutron flux we used the measurements taken in New York (see Fig. 9 taken from Fig. 4 in [21]). We note that even after correcting for altitude, location, and solar activity, the flux of low energy neutrons varies because of differences in the local environment [21] and we have therefore assumed a 30% uncertainty in the overall normalization of the flux. For the ^{38}Ar(n, γ)^{39}Ar cross section we have used the ENDF/B-VIII.I values [44] (shown in Fig. 9) which agrees well with experimental data at thermal energies [70,72]. Because of the low abundance of ^{38}Ar the contribution to the total production rate [(1.1 ± 0.3) atoms/(kg$_{\rm Ar}$day)] is negligible.

The estimates for each of these alternate production mechanisms for ^{39}Ar is summarized in Table V, with fast neutrons contributing 73% of the total production rate of ^{39}Ar at sea level. As partial verification, one can compare the estimates of the total ^{39}Cl production rate to an experimental measurement of the production rate of ^{39}Cl in argon gas exposed at sea level [31]. Summing up the contributions from fast neutrons [(173 ± 71) atoms(^{39}Cl)/(kg$_{\rm Ar}$day) through ^{40}Ar (n, d)^{39}Cl] with the alternate mechanisms listed in Table V, one obtains a total production rate of (369 ± 76) atoms(^{39}Cl)/(kg$_{\rm Ar}$day) which is in relatively good agreement with the experimentally measured (288 ± 29) atoms(^{39}Cl)/(kg$_{\rm Ar}$day).

Thus the total cosmic ray production rate at sea level is expected to be (1048 ± 133) atoms/(kg$_{\rm Ar}$day) for ^{39}Ar, which corresponds to a cosmic ray activation rate of $(8.6 \pm 1.1) \times 10^{-8}$ Bq/(kg$_{\rm Ar}$day) and a saturated equilibrium activity of $(1.21 \pm 0.15) \times 10^{-3}$ Bq/kg$_{\rm Ar}$. Note that the equilibrium activity at sea level is lower than the measured level of ^{39}Ar in the atmosphere because the total rate in the atmosphere is dominated by the production at high altitudes, where the neutron flux is significantly higher.

B. Alternate ^{37}Ar production mechanisms

1. ^{40}Ar *(γ, 3n)*^{37}Ar *and* ^{40}Ar *(p, p3n)*^{37}Ar

We are not aware of any existing measurements of either the ^{40}Ar (γ, 3n)^{37}Ar or the ^{40}Ar (p, p3n)^{37}Ar cross section. For the production rate from gammas we used the cross section from TALYS (shown in Fig. 8), while for proton-induced reactions we have used the production rates obtained with the TALYS and INCL++ ^{40}Ar (n, 4n)^{37}Ar cross sections. As above, where multiple flux or cross-section estimates exist we have used the mean and sample standard deviation of the calculated production rates as our estimates of the central value and uncertainty. We estimate a sea-level production rate of (3.5 ± 0.7) atoms/(kg$_{\rm Ar}$day) and (1.3 ± 0.4) atoms/(kg$_{\rm Ar}$day) from ^{40}Ar (γ, 3n)^{37}Ar and ^{40}Ar (p, p3n)^{37}Ar, respectively.

2. ^{36}Ar(n, γ)^{37}Ar

In AAr, ^{37}Ar can also be produced through the capture of thermal and epi-thermal neutrons on ^{36}Ar. For the ^{36}Ar(n, γ)^{37}Ar cross section we have used the ENDF/B-VII.I values [44] (shown in Fig. 9) which agrees well with experimental data at thermal energies [71,72], though recent measurements at higher energies (Maxwellian kT $\approx$47 keV) indicate that the cross sections could be significantly lower than previous estimates [72]. This production channel produces a significant contribution to the total production rate of (36 ± 11) atoms/(kg$_{\rm Ar}$day) at sea level. Note that the abundance of ^{36}Ar in argon from underground sources is reduced by roughly a factor of 40, and hence the production of ^{37}Ar from neutron captures in UAr is < 1 atom/kg$_{\rm Ar}$/d.

3. ^{38}Ar(n, 2n)^{37}Ar, ^{38}Ar(γ, n)^{37}Ar, *and* ^{38}Ar(p, pn)^{37}Ar

All of the direct production mechanisms of ^{39}Ar from ^{40}Ar also apply to the production of ^{37}Ar from ^{38}Ar in AAr. We are not aware of any experimental measurements of the cross sections on ^{38}Ar except for ^{38}Ar (γ, n)^{37}Ar [80] which is roughly the same as the ^{40}Ar (γ, n)^{39}Ar cross section. We have therefore estimated the production rate from reactions on ^{38}Ar by taking the sum of the production rates from all direct ^{40}Ar (x, y)^{39}Ar mechanisms [(679 ± 85) atoms/(kg$_{\rm Ar}$day)] and scaling it by the abundance of ^{38}Ar in AAr (0.000629). This is perhaps an overestimation because of the fact that ^{38}Ar has a magic number of neutrons and may therefore be expected to have lower cross sections for the ejection of a neutron than ^{40}Ar, but the contribution is in any case negligible [(0.43 ± 0.05) atoms/(kg$_{\rm Ar}$day)].

TABLE VI. Total cosmogenic production rates of ^{37}Ar at sea level. The first row is the estimate from fast neutrons based on the measurement presented in this work, while the other rows are best estimates made from existing experimental data and models.

Reaction	Estimated ^{37}Ar production rate [atoms/(kg_{Ar}day)]	Fraction of total UAr (%)	Fraction of total AAr (%)
^{40}Ar (n, 4n)^{37}Ar	51.0 ± 7.4	90.0	55.5
^{40}Ar (γ, 3n)^{37}Ar	3.5 ± 0.7	6.1	3.8
^{40}Ar (p, p3n)^{37}Ar	1.3 ± 0.4	2.3	1.4
^{36}Ar(n, γ)^{37}Ar	0.9 ± 0.3 (UAr) 36 ± 11 (AAr)	1.6	38.9
^{38}Ar(n, 2n)^{37}Ar+ ^{38}Ar(γ, n)^{37}Ar+ ^{38}Ar(p, pn)^{37}Ar	<0.05 (UAr) 0.43 ± 0.05 (AAr)	<0.1	0.5
Total	56.7 ± 7.5 (UAr) 92 ± 13 (AAr)	100	100

The estimates for each of these alternate production mechanisms for ^{37}Ar are summarized in Table VI. The total cosmic ray production rate at sea level is expected to be (56.7 ± 7.5) atoms/(kg_{Ar}day) for ^{37}Ar in underground argon and (92 ± 13) atoms/(kg_{Ar}day) for ^{37}Ar in atmospheric argon. These numbers correspond to a cosmic ray activation rate of $(1.30 \pm 0.17) \times 10^{-5}$ Bq/(kg_{Ar}day) for UAr and $(2.11 \pm 0.30) \times 10^{-5}$ Bq/(kg_{Ar}day) for AAr, and a saturated equilibrium activity of $(6.56 \pm 0.87) \times 10^{-4}$ Bq/kg_{Ar}, $(1.06 \pm 0.15) \times 10^{-3}$ Bq/kg_{Ar}, respectively.

VIII. SUMMARY AND DISCUSSION

We have made the first experimental measurement of the production rate of ^{39}Ar and ^{37}Ar from fast neutron interactions in argon. This measurement was enabled by the ability to directly measure the β and electron-capture decays that are not detectable with standard methods only sensitive to γ rays from activation products. Including uncertainties in the cross-section models and the cosmogenic neutron flux we obtained a production rate of (759 ± 128) atoms/(kg_{Ar}day) for ^{39}Ar, and (51.0 ± 7.4) atoms/(kg_{Ar}day) for ^{37}Ar from cosmogenic neutrons at sea level. Combined with calculated estimates of other production mechanisms, we obtain a total cosmic ray production rate at sea level of (1048 ± 133) atoms/(kg_{Ar}day) for ^{39}Ar, and (92 ± 13) atoms/(kg_{Ar}day) for ^{37}Ar in atmospheric argon [(56.7 ± 7.5) atoms/(kg_{Ar}day) for ^{37}Ar in UAr].

These results are most relevant to argon-based dark matter detectors where ^{39}Ar is the dominant background and lowering the rate of ^{39}Ar can reduce energy thresholds and improve sensitivity. The argon extracted from underground and used as the target for the DarkSide-50 experiment was measured to have an ^{39}Ar rate of 7.3×10^{-4} Bq/kg_{Ar} [15], but it is thought that a large fraction of the residual ^{39}Ar was from an air infiltration during the purification of the underground gas. Thus it is possible that the measured activity is only an upper limit, and the true rate of ^{39}Ar in UAr could be as low as 3×10^{-5} Bq/kg_{Ar} [84]. For future multiton dark matter detectors low levels of ^{39}Ar are even more critical, and efforts will be made to avoid any contamination of the underground argon with the atmosphere [85]. At this possibly lower intrinsic ^{39}Ar rate, cosmogenic activation of the underground argon (once it is extracted to the surface) is potentially a significant contributor to the overall background. The results from this paper, scaled by the cosmic ray flux at the relevant altitudes and locations, can be used to calculate the experiment-specific maximum duration UAr can spend above ground during extraction, purification, storage, and transportation. We note that the measured sea-level activation rate of ^{39}Ar in this paper [$(8.6 \pm 1.1) \times 10^{-8}$ Bq/(kg_{Ar}day)] is nearly an order of magnitude larger than previous estimates based on semiempirical calculations $(0.5 - 1.5) \times 10^{-8}$ Bq/(kg_{Ar}day) [50].

Finally, these results can also be used to estimate the total equilibrium rate of ^{39}Ar and ^{37}Ar in the atmosphere. This is potentially useful for establishing baseline values for radioactive dating and nuclear activity monitoring, as well as evaluating the constancy of cosmic radiation [51].

ACKNOWLEDGMENTS

This work was supported by the Laboratory Directed Research and Development Program at Pacific Northwest National Laboratory, a multiprogram national laboratory operated by Battelle for the U.S. Department of Energy under Contract No. DE-AC05-76RL01830, and also the U.S. Department of Energy, Office of Science, Office of Nuclear Physics under Los Alamos National Laboratory Award No. LANLE9BW. This work benefited from the use of the Los Alamos Neutron Science Center, funded by the U.S. Department of Energy under Contract No. DE-AC52-06NA25396 and we would like to thank Steve Wender for his assistance with the beam exposure.

[1] C. Rubbia, M. Antonello, P. Aprili, B. Baibussinov, M. B. Ceolin, L. Barze, P. Benetti, E. Calligarich, N. Canci, F. Carbonara *et al.*, Underground operation of the ICARUS T600 LAr-TPC: First results, J. Instrum. **6**, P07011 (2011).

[2] B. Abi, R. Acciarri, M. Acero, M. Adamowski, C. Adams, D. Adams, P. Adamson, M. Adinolfi, Z. Ahmad, C. Albright *et al.*, The DUNE far detector interim design report volume 1: Physics, technology, and strategies, arXiv:1807.10334.

[3] M. Agostini, M. Allardt, A. Bakalyarov, M. Balata, I. Barabanov, L. Baudis, C. Bauer, E. Bellotti, S. Belogurov, S. Belyaev *et al.*, Background-free search for neutrinoless double-β decay of 76 Ge with GERDA, Nature (London) **544**, 47 (2017).

[4] P. Benetti, R. Acciarri, F. Adamo, B. Baibussinov, M. Baldo-Ceolin, M. Belluco, F. Calaprice, E. Calligarich, M. Cambiaghi, F. Carbonara *et al.*, First results from a dark matter search with liquid argon at 87 K in the Gran Sasso underground laboratory, Astropart. Phys. **28**, 495 (2008).

[5] P. Agnes, I. Albuquerque, T. Alexander, A. Alton, G. Araujo, M. Ave, H. Back, B. Baldin, G. Batignani, K. Biery *et al.*, Darkside-50 532-day dark matter search with low-radioactivity argon, Phys. Rev. D **98**, 102006 (2018).

[6] P.-A. Amaudruz, M. Baldwin, M. Batygov, B. Beltran, C. Bina, D. Bishop, J. Bonatt, G. Boorman, M. G. Boulay, B. Broerman *et al.*, First Results from the DEAP-3600 Dark Matter Search with Argon at SNOLAB, Phys. Rev. Lett. **121**, 071801 (2018).

[7] H. Loosli and H. Oeschger, Detection of ^{39}Ar in atmospheric argon, Earth Planet. Sci. Lett. **5**, 191 (1968).

[8] P. Benetti, F. Calaprice, E. Calligarich, M. Cambiaghi, F. Carbonara, F. Cavanna, A. Cocco, F. Di Pompeo, N. Ferrari, G. Fiorillo *et al.*, Measurement of the specific activity of ^{39}Ar in natural argon, Nucl. Instrum. Methods Phys. Res. Sect. A **574**, 83 (2007).

[9] R. Purtschert, M. Kaliowski, J. Wieslander, X. Blanchard, R. Riedmann, L. Raghoo, J. Kusmierczyk-Michulec, H. Gheddou, and Y. Tomita, Ar-37, Be-7, and Xe-133 in the atmosphere, in CTBT Science and Technology 2017 Conference (CTBT, Vienna, 2017), Sec. T1.3-O2.

[10] A. Barabash, R. Saakyan, and V. Umatov, On concentration of ^{42}Ar in the Earth's atmosphere, Nucl. Instrum. Methods Phys. Res. Sect. A **839**, 39 (2016).

[11] M. Agostini, M. Allardt, E. Andreotti, A. Bakalyarov, M. Balata, I. Barabanov, M. B. Heider, N. Barros, L. Baudis, C. Bauer *et al.*, The background in the $0\nu\beta\beta$ experiment GERDA, Eur. Phys. J. C **74**, 2764 (2014).

[12] J. K. Böhlke, Variation in the terrestrial isotopic composition and atomic weight of argon (IUPAC technical report), Pure Appl. Chem. **86**, 1421 (2014).

[13] J. Chen, Nuclear Data Sheets for A = 39, Nucl. Data Sheets **149**, 1 (2018).

[14] P. Agnes, T. Alexander, A. Alton, K. Arisaka, H. Back, B. Baldin, K. Biery, G. Bonfini, M. Bossa, A. Brigatti *et al.*, First results from the DarkSide-50 dark matter experiment at Laboratori Nazionali del Gran Sasso, Phys. Lett. B **743**, 456 (2015).

[15] P. Agnes, L. Agostino, I. Albuquerque, T. Alexander, A. Alton, K. Arisaka, H. Back, B. Baldin, K. Biery, G. Bonfini *et al.*, Results from the first use of low radioactivity argon in a dark matter search, Phys. Rev. D **93**, 081101 (2016).

[16] P. Agnes, I. Albuquerque, T. Alexander, A. Alton, G. Araujo, D. Asner, M. Ave, H. Back, B. Baldin, G. Batignani *et al.*, Low-Mass Dark Matter Search with the DarkSide-50 Experiment, Phys. Rev. Lett. **121**, 081307 (2018).

[17] H. O. Back, F. Calaprice, C. Condon, E. de Haas, R. Ford, C. Galbiati, A. Goretti, T. Hohman, A. Inanni, B. Loer *et al.*, First large scale production of low radioactivity argon from underground sources, arXiv:1204.6024.

[18] J. Cameron, J. Chen, B. Singh, and N. Nica, Nuclear data sheets for A = 37, Nucl. Data Sheets **113**, 365 (2012).

[19] C. E. Aalseth, A. R. Day, D. A. Haas, E. W. Hoppe, B. J. Hyronimus, M. E. Keillor, E. K. Mace, J. L. Orrell, A. Seifert, and V. T. Woods, Measurement of ^{37}Ar to support technology for on-site inspection under the comprehensive nuclear-test-ban treaty, Nucl. Instrum. Methods Phys. Res. Sect. A **652**, 58 (2011).

[20] R. A. Riedmann and R. Purtschert, Natural ^{37}Ar concentrations in soil air: Implications for monitoring underground nuclear explosions, Environ. Sci. Technol. **45**, 8656 (2011).

[21] M. Gordon, P. Goldhagen, K. Rodbell, T. Zabel, H. Tang, J. Clem, and P. Bailey, Measurement of the flux and energy spectrum of cosmic-ray induced neutrons on the ground, IEEE Trans. Nucl. Sci. **51**, 3427 (2004).

[22] P. W. Lisowski and K. F. Schoenberg, The Los Alamos Neutron Science Center, Nucl. Instrum. Methods Phys. Res. Sect. A **562**, 910 (2006).

[23] B. Takala, *The ICE House* (Los Alamos Science, Los Alamos National Laboratory, Los Alamos, 2006).

[24] C. Aalseth, A. Day, E. Hoppe, T. Hossbach, B. Hyronimus, M. Keillor, K. Litke, E. Mintzer, A. Seifert, and G. Warren, Design and construction of a low-background, internal-source proportional counter, J. Radiol. Nucl. Chem. **282**, 233 (2009).

[25] J. Hall, C. E. Aalseth, R. M. Bonicalzi, J. M. Brandenberger, A. R. Day, P. H. Humble, E. K. Mace, M. E. Panisko, and A. Seifert, ^{39}Ar/Ar measurements using ultra-low background proportional counters, Appl. Radiat. Isot. **107**, 187 (2016).

[26] E. K. Mace, Sensitivity and detection limits for measuring low-levels of argon radioisotopes (^{37}Ar and ^{39}Ar) using ultra-low-background proportional counters (Low-Radioactivity Underground Argon Workshop, Richland, Washington, 2018), http://doi.org/10.5281/zenodo.1239118.

[27] S. MacMullin, M. Boswell, M. Devlin, S. R. Elliott, N. Fotiades, V. E. Guiseppe, R. Henning, T. Kawano, B. H. LaRoque, R. O. Nelson, and J. M. O'Donnell, Partial γ-ray production cross sections for (n,xn γ) reactions in natural argon at 1–30 MeV, Phys. Rev. C **85**, 064614 (2012).

[28] P. R. Gray, A. R. Zander, and T. G. Ebrey, Activation cross sections for reactions of argon with 14.7 MeV neutrons, Nucl. Phys. **62**, 172 (1965).

[29] L. Husain and P. Kuroda, 14.8 MeV neutron activation cross-sections of argon, J. Inorg. Nucl. Chem. **30**, 355 (1968).

[30] N. Ranakumar, E. Karttunen, and R. Fink, Thermal and 14.4 MeV neutron activation cross sections of argon, Nucl. Phys. A **128**, 333 (1969).

[31] M. Rama and M. Honda, Cosmic-ray-induced radioactivity in terrestrial materials, J. Geophys. Res. **66**, 3533 (1961).

[32] R. Silberberg and C. H. Tsao, Partial cross-sections in high-energy nuclear reactions, and astrophysical applications. I. targets with Z $\leqslant$ 28, Astrophys. J. Suppl. Ser. **25**, 315 (1973).

[33] R. Silberberg and C. H. Tsao, Partial cross-sections in high-energy nuclear reactions, and astrophysical applications. II. Targets heavier than nickel, Astrophys. J. Suppl. Ser. **25**, 335 (1973).

[34] R. Silberberg and C. Tsao, Cross sections for (p, xn) reactions, and astrophysical applications, Astrophys. J. Suppl. Ser. **35**, 129 (1977).

[35] R. Silberberg, C. Tsao, and J. R. Letaw, Improved cross section calculations for astrophysical applications, Astrophys. J. Suppl. Ser. **58**, 873 (1985).

[36] R. Silberberg and C. Tsao, Spallation processes and nuclear interaction products of cosmic rays, Phys. Rep. **191**, 351 (1990).

[37] R. Silberberg, C. Tsao, and A. Barghouty, Updated partial cross sections of proton-nucleus reactions, Astrophys. J. **501**, 911 (1998).

[38] C. Tsao, R. Silberberg, A. Barghouty, and M. Mattson, YIELDX: *Semi-Empirical Cross-Section Routines* (Roanoke College, Salem, 1996).

[39] C. Martoff and P. Lewin, COSMO-a program to estimate spallation radioactivity produced in a pure substance by exposure to cosmic radiation on the earth, Comput. Phys. Commun. **72**, 96 (1992).

[40] J. Back and Y. A. Ramachers, ACTIVIA: Calculation of isotope production cross-sections and yields, Nucl. Instrum. Methods Phys. Res. Sect. A **586**, 286 (2008).

[41] A. Boudard, J. Cugnon, J.-C. David, S. Leray, and D. Mancusi, New potentialities of the liege intranuclear cascade model for reactions induced by nucleons and light charged particles, Phys. Rev. C **87**, 014606 (2013).

[42] A. Kelic and K.-H. Schmidt, The de-excitation code ABLA07, *Proceedings of Joint ICTP-IAEA Advanced Workshop on Model Codes for Spallation Reactions* (ICTP, Trieste, 2008), p. 181.

[43] A. Koning, S. Hilaire, and M. Duijvestijn, TALYS-1.0, in *Proceedings of the International Conference on Nuclear Data for Science and Technology*, April 22–27, 2007, edited by O. Bersillon, F. Gunsing, E. Bauge, R. Jacqmin, and S. Leray (Springer-Verlag, Berlin/Heidelberg, 2008), p. 211.

[44] M. Chadwick, M. Herman, P. Obložinsk, M. E. Dunn, Y. Danon, A. Kahler, D. L. Smith, B. Pritychenko, G. Arbanas, R. Arcilla *et al.*, ENDF/B-VII. 1 nuclear data for science and technology: Cross sections, covariances, fission product yields and decay data, Nucl. Data Sheets **112**, 2887 (2011).

[45] P. McLaughlin and V. Pronyaev, MENDL-2P. Proton reaction data library for nuclear activation (medium energy nuclear data library) Technical Report (International Atomic Energy Agency, Vienna, 1998).

[46] A. J. Koning and D. Rochman, Modern nuclear data evaluation with the TALYS code system, Nucl. Data Sheets **113**, 2841 (2012).

[47] J. Back and Y. Ramachers, https://github.com/UniversityofWarwick/ACTIVIA.

[48] D. Mancusi, A. Boudard, J. Cugnon, J.-C. David, P. Kaitaniemi, and S. Leray, Extension of the liège intranuclear-cascade model to reactions induced by light nuclei, Phys. Rev. C **90**, 054602 (2014).

[49] A. Koning, S. Hilaire, and M. Duijvestijn, Computer code TALYS-1.9, http://www.talys.eu/download-talys/.

[50] C. Aalseth, F. Acerbi, P. Agnes, I. Albuquerque, T. Alexander, A. Alici, A. Alton, P. Antonioli, S. Arcelli, R. Ardito *et al.*, DarkSide-20k: A 20 tonne two-phase LAr TPC for direct dark matter detection at LNGS, Eur. Phys. J. Plus **133**, 131 (2018).

[51] H. Loosli, H. Oeschger, and W. Wiest, Argon 37, Argon 39, and Krypton 81 in the atmosphere and tracer studies based on these isotopes, J. Geophys. Res. **75**, 2895 (1970).

[52] J. Meija, T. B. Coplen, M. Berglund, W. A. Brand, P. De Bièvre, M. Gröning, N. E. Holden, J. Irrgeher, R. D. Loss, T. Walczyk *et al.*, Isotopic compositions of the elements 2013 (IUPAC technical Report), Pure Appl. Chem. **88**, 293 (2016).

[53] R. Williams, C. Aalseth, J. Brandenberger, A. Day, E. Finn, E. Fuller, E. Hoppe, P. Humble, M. Keillor, E. Mace, A. Myers, C. Overman, M. Panisko, A. Seifert, and S. White, Development of a low-level ^{39}Ar calibration standard – Analysis by absolute gas counting measurements augmented with simulation, Appl. Radiat. Isot. **126**, 243 (2017).

[54] S. Wender, S. Balestrini, A. Brown, R. Haight, C. Laymon, T. Lee, P. Lisowski, W. McCorkle, R. Nelson, W. Parker *et al.*, A fission ionization detector for neutron flux measurements at a spallation source, Nucl. Instrum. Methods Phys. Res. Sect. A **336**, 226 (1993).

[55] A. D. Carlson, S. Chiba, F. J. Hambsch, N. Olsson, and A. N. Smirnov, The 238U(n,f) Cross Section, Technical Report, International Atomic Energy Agency (IAEA, Vienna, 1997), http://inis.iaea.org/search/search.aspx?orig_q=RN:28055848.

[56] S. Agostinelli, J. Allison, K. Amako, J. Apostolakis, H. Araujo, P. Arce, M. Asai, D. Axen, S. Banerjee, G. Barrand *et al.*, GEANT4—a simulation toolkit, Nucl. Instrum. Methods Phys. Res. Sect. A **506**, 250 (2003).

[57] J. Allison, K. Amako, J. Apostolakis, P. Arce, M. Asai, T. Aso, E. Bagli, A. Bagulya, S. Banerjee, G. Barrand *et al.*, Recent developments in GEANT4, Nucl. Instrum. Methods Phys. Res. Sect. A **835**, 186 (2016).

[58] R. Brodzinski and N. Wogman, High-energy proton spallation of argon, Phys. Rev. C **1**, 1955 (1970).

[59] J.-L. Reyss, Y. Yokoyama, and F. Guichard, Production cross sections of ^{26}Al, ^{22}Na, ^{7}Be from argon and of ^{10}Be, ^{7}Be from nitrogen: Implications for production rates of ^{26}Al and ^{10}Be in the atmosphere, Earth Planet. Sci. Lett. **53**, 203 (1981).

[60] B. T. Cleveland, T. Daily, R. Davis, Jr., J. R. Distel, K. Lande, C. Lee, P. S. Wildenhain, and J. Ullman, Measurement of the solar electron neutrino flux with the Homestake chlorine detector, Astrophys. J. **496**, 505 (1998).

[61] R. M. Williams, C. E. Aalseth, T. W. Bowyer, A. R. Day, E. S. Fuller, D. A. Haas, J. C. Hayes, E. W. Hoppe, P. H. Humble, M. E. Keillor *et al.*, Development of a low-level ^{37}Ar calibration standard, Appl. Radiat. Isot. **109**, 430 (2016).

[62] A. Koning, D. Rochman, and S. van der Marck, Extension of TALYS to 1 GeV, Nucl. Data Sheets **118**, 187 (2014).

[63] W. N. Hess, H. W. Patterson, R. Wallace, and E. L. Chupp, Cosmic-ray neutron energy spectrum, Phys. Rev. **116**, 445 (1959).

[64] T. Armstrong, K. Chandler, and J. Barish, Calculations of neutron flux spectra induced in the earth's atmosphere by galactic cosmic rays, J. Geophys. Res. **78**, 2715 (1973).

[65] J. F. Ziegler, Terrestrial cosmic rays, IBM J. Res. Dev. **40**, 19 (1996).

[66] D. Desilets and M. Zreda, On scaling cosmogenic nuclide production rates for altitude and latitude using cosmic-ray measurements, Earth Planet. Sci. Lett. **193**, 213 (2001).

[67] T. Sato, EXcel-based program for calculating atmospheric cosmic-ray spectrum (EXPACS), v4.04, https://phits.jaea.go.jp/expacs/.

[68] I. Diggory, J. Hook, I. Jenkins, and K. Turver, The momentum spectra of nuclear active particles in the cosmic radiation at sea level. I. Experimental data, J. Phys. A **7**, 741 (1974).

[69] J. Ziegler, The background in detectors caused by sea level cosmic rays, Nucl. Instrum. Methods Phys. Res. **191**, 419 (1981).

[70] S. Katcoff, Thermal neutron capture cross section of A^{40} and observation of A^{42}, Phys. Rev. **87**, 886 (1952).

[71] G. McMurtrie and D. Crawford, The thermal neutron-capture cross section of A^{36}, Phys. Rev. **77**, 840 (1950).

[72] M. Tessler, M. Paul, S. Halfon, B. S. Meyer, R. Pardo, R. Purtschert, K. E. Rehm, R. Scott, M. Weigand, L. Weissman, S. Almaraz-Calderon, M. L. Avila, D. Baggenstos, P. Collon, N. Hazenshprung, Y. Kashiv, D. Kijel, A. Kreisel, R. Reifarth, D. Santiago-Gonzalez, A. Shor, I. Silverman, R. Talwar, D. Veltum, and R. Vondrasek, Stellar Ar 36,38 (n, γ) Ar 37, 39 Reactions and Their Effect on Light Neutron-Rich Nuclide Synthesis, Phys. Rev. Lett. **121**, 112701 (2018).

[73] S. Charalambus, Nuclear transmutation by negative stopped muons and the activity induced by the cosmic-ray muons, Nucl. Phys. A **166**, 145 (1971).

[74] A. Bertin, A. Vitale, and A. Placci, Nuclear capture of muons in argon and neon, Phys. Rev. A **7**, 2214 (1973).

[75] M. Tanabashi *et al.*, Review of particle physics, Phys. Rev. D **98**, 030001 (2018).

[76] A. Klinskikh, S. Brianson, V. Brudanin, V. Egorov, C. Petitjean, and M. Shirchenko, Muon capture in Ar. The muon lifetime and yields of Cl isotopes, Bull. Russ. Acad. Sci.: Phys. **72**, 735 (2008).

[77] M. Pârvu, A. Chiriacescu, and I. Lazanu, Short analysis of cosmogenic production of radioactive isotopes in argon as target for the next neutrino experiments, Radiat. Phys. Chem. **152**, 129 (2018).

[78] T. Sato, Analytical model for estimating the zenith angle dependence of terrestrial cosmic ray fluxes, PloS one **11**, e0160390 (2016).

[79] J. M. Ryan, M. C. Jennings, M. D. Radwin, A. D. Zych, and R. S. White, Atmospheric gamma ray angle and energy distributions from sea level to 3.5 g/cm^2 and 2 to 25 MeV, J. Geophys. Res. [Space Phys.] **84**, 5279 (1979).

[80] D. Ehhalt, R. Kosiek, and R. Pfeiffer, Zum Kernphotoeffekt am Ar^{40} und Ar^{38}, Z. Phys. **187**, 210 (1965).

[81] J. Jury, J. Lodge, K. Lokan, N. Sherman, and R. Gellie, Photoneutron Disintegration of ^{40}Ar, Can. J. Phys. **51**, 1176 (1973).

[82] R. Sutton, P. Allen, M. Thompson, and E. Muirhead, The photodisintegration of ^{40}Ar, Nucl. Phys. A **398**, 415 (1983).

[83] K. Nagatsu, A. Kubodera, and K. Suzuki, Excitation function measurements of ^{40}Ar (p, 3n) ^{38}K, ^{40}Ar (p, 2pn) ^{38}Cl and ^{40}Ar (p, 2p) ^{39}Cl reactions, Appl. Radiat. Isot. **50**, 389 (1999).

[84] A. Renshaw, Urania: Extraction of UAr for DarkSide-20k, Low-Radioactivity Underground Argon Workshop, Richland, Washington, http://doi.org/10.5281/zenodo.1239080 (2018).

[85] H. O. Back, Device and method for testing underground argon, United States of America Patent No. US 10,126,280 (2018).